



**HAL**  
open science

# Transparent Porous ZnO|Metal Complex Nanostructured Materials: Application to Electrocatalytic CO<sub>2</sub> Reduction

Julian Guerrero, Nathanaelle Schneider, Fabienne Dumoulin, Daniel Lincot, Umit Isci, Negar Naghavi, Marc Robert

## ► To cite this version:

Julian Guerrero, Nathanaelle Schneider, Fabienne Dumoulin, Daniel Lincot, Umit Isci, et al.. Transparent Porous ZnO|Metal Complex Nanostructured Materials: Application to Electrocatalytic CO<sub>2</sub> Reduction. ACS Applied Nano Materials, 2023, 6 (12), pp.10626-10635. 10.1021/acsnm.3c01591 . hal-04158858

**HAL Id: hal-04158858**

**<https://cnrs.hal.science/hal-04158858v1>**

Submitted on 11 Jul 2023

**HAL** is a multi-disciplinary open access archive for the deposit and dissemination of scientific research documents, whether they are published or not. The documents may come from teaching and research institutions in France or abroad, or from public or private research centers.

L'archive ouverte pluridisciplinaire **HAL**, est destinée au dépôt et à la diffusion de documents scientifiques de niveau recherche, publiés ou non, émanant des établissements d'enseignement et de recherche français ou étrangers, des laboratoires publics ou privés.

This document is confidential and is proprietary to the American Chemical Society and its authors. Do not copy or disclose without written permission. If you have received this item in error, notify the sender and delete all copies.

**Transparent hybrid materials (metal complexes/ZnO nanostructures): synergetic effects in electrocatalytic reactions, application to CO2 reduction**

Journal:	<i>ACS Applied Nano Materials</i>
Manuscript ID	an-2023-015912
Manuscript Type:	Article
Date Submitted by the Author:	10-Apr-2023
Complete List of Authors:	Guerrero, Julian; University of Paris, Chemistry; IPVF Schneider, Nathanaelle; IPVF Dumoulin, Fabienne; Acibadem Universitesi, Biomedical Engineering Department Lincot, Daniel; IPVF Isci, Umit; Marmara University, Department of Metallurgical & Materials Engineering Naghavi, Negar; CNRS, E2P2L, UMI 3464 Robert, Marc; University of Paris, Chemistry

SCHOLARONE™  
Manuscripts

1  
2  
3 **Transparent hybrid materials (metal complexes/ZnO nanostructures):**  
4  
5  
6 **synergetic effects in electrocatalytic reactions, application to CO<sub>2</sub> reduction**  
7  
8  
9

10 *Julian Guerrero,<sup>a,b</sup> Nathanaelle Schneider,<sup>b</sup> Fabienne Dumoulin,<sup>c</sup> Daniel Lincot,<sup>b</sup> Umit Isci,<sup>d\*</sup>*  
11  
12 *Negar Naghavi,<sup>b\*</sup> Marc Robert<sup>a,e\*</sup>*  
13  
14  
15

16  
17  
18 <sup>a</sup> Laboratoire d'Electrochimie Moléculaire, Université de Paris, CNRS, F-75006 Paris, France  
19

20 <sup>b</sup> Institut Photovoltaïque d'Île-de-France (IPVF), CNRS, UMR 9006, 91120 Palaiseau, France  
21

22 <sup>c</sup> Acıbadem Mehmet Ali Aydınlar University, Faculty of Engineering and Natural Sciences,  
23  
24 Biomedical Engineering Department, 34752 Ataşehir, Istanbul, Türkiye  
25

26  
27 <sup>d</sup> Marmara University, Faculty of Technology, Department of Metallurgical & Materials  
28  
29  
30 Engineering, 34722 Istanbul, Türkiye  
31

32  
33 <sup>e</sup> Institut Universitaire de France (IUF), F-75005, Paris, France  
34  
35  
36  
37  
38  
39  
40  
41  
42  
43  
44  
45  
46  
47  
48  
49  
50  
51  
52  
53  
54  
55  
56  
57  
58  
59  
60

## Abstract

We developed a simple and versatile approach for the electrochemical growth of hybrid ZnO/molecular catalyst nanostructured layers. A metal oxide/catalyst hybrid nanoporous layer with a sponge-like structure at the nanoscale and multiscale 3D hierarchical structures based on nanoporous ZnO layers grown on zinc oxide nanorods have been obtained. The thickness and structure of the hybrid nanoporous layer as well as the catalyst concentration can be tuned. This method allowed for the introduction of water soluble molecular catalysts based on porphyrin and/or phthalocyanine derivatives into the ZnO matrix with a homogeneous distribution of the complex. As an illustrative example, combining hybrid ZnO with a very low concentration of an encapsulated Co-based molecular catalyst inside the oxide layer resulted in a 97% catalytic response toward CO<sub>2</sub> reduction to CO with large currents, highlighting the excellent electrocatalytic activities of such layers, which combine porosity, electronic conductivity and synergetic properties from its components.

**Keywords:** Hybrid material, nanomaterials, molecular catalyst, cobalt complex, electrochemical CO<sub>2</sub> reduction

## Introduction

Inorganic–organic hybrid materials are a class of compounds gaining more and more interest due to their distinct chemical and physical properties.<sup>[1]</sup> They are disordered physical-chemical systems in which inorganic components (metal ions, oxides, sulfides, non-metallic elements, etc.) and organic components (organic molecules, ligands, biomolecules, polymers, etc.) are brought together by specific interactions resulting in a synergistic enhancement of their functional properties,<sup>[2]</sup> opening up new fields of properties and functional capabilities that would not be possible with just one of the components. This growing field of research has found

1  
2  
3 a wide range of applications such as energy storage, high performance capacitors, solar cells,  
4 catalysis and photocatalysis.<sup>[3,4]</sup> Otherwise, electrocatalytic reactions such as reduction of CO<sub>2</sub>  
5 (CO<sub>2</sub>RR) is an appealing option for storing renewable electricity and producing valuable  
6 chemicals and fuels such as CO, HCOOH, CH<sub>4</sub>, CH<sub>3</sub>OH, or CH<sub>3</sub>CH<sub>2</sub>OH,<sup>[5]</sup> in a sustainable  
7 manner. The reaction is not only a thermodynamically uphill process, but also suffers from slow  
8 kinetics. Moreover, poor catalytic selectivity and high overpotential continue to limit efficiency  
9 and upscaling of CO<sub>2</sub> electroreduction.<sup>[6]</sup> The search for increased activity, selectivity and  
10 stability of catalysts requires new systems. The combination of organic and inorganic hybrid  
11 nanostructured materials can play a significant role in this direction. While using nanostructured  
12 or high surface area catalysts can significantly improve surface reactivity by making a  
13 significant fraction of the reactive sites available for catalysis, the use of organic-inorganic  
14 hybrid materials can open up the possibility of addressing new properties of catalysts that would  
15 otherwise be inaccessible using purely organic or inorganic materials.

16  
17  
18  
19  
20  
21  
22  
23  
24  
25  
26  
27  
28  
29  
30  
31  
32  
33 Currently, a variety of earth-abundant metal-based molecular catalysts have been identified  
34 reporting high selectivity for the CO<sub>2</sub> reduction reaction.<sup>[5,7-9]</sup> Among examples, cobalt  
35 phthalocyanine has been identified as good electrocatalyst for CO<sub>2</sub>RR owing to its high  
36 selectivity and activity for CO production.<sup>[10,11]</sup> Besides, oxide-derived metal based materials  
37 such as CuO, Cu<sub>2</sub>O,<sup>[12-15]</sup> Ag<sub>2</sub>O,<sup>[16,17]</sup> NiO,<sup>[18,19]</sup> and TiO<sub>2</sub>,<sup>[20,22]</sup> have been successfully  
38 demonstrated to be active and selective catalysts for CO<sub>2</sub> reduction. ZnO, a low toxic compound,  
39 is an oxide-derived non-noble metal with promising optical,<sup>[23]</sup> electronic,<sup>[24]</sup> photovoltaic,<sup>[25,27]</sup>  
40 and catalytic properties.<sup>[28-31]</sup> Recently a maximum faradaic efficiency (FE) of 92% for CO<sub>2</sub> to  
41 CO conversion has been reported for a nanoporous ZnO.<sup>[32]</sup> However, the catalytic system  
42 suffered from degradation issues due to morphological change during CO<sub>2</sub> reduction in aqueous  
43 media.

44  
45  
46  
47  
48  
49  
50  
51  
52  
53  
54  
55  
56  
57  
58  
59  
60  
ZnO has the distinct advantage of being easily prepared in high quality and in a wide range of  
nanostructures, such as nanorods,<sup>[33,34]</sup> nanotubes,<sup>[35,36]</sup> nanobelts,<sup>[37,38]</sup> via solution routes such

1  
2  
3 as chemical bath deposition (CBD)/dip coating,<sup>[9]</sup> chemical vapor deposition (CVD)/spray  
4  
5 pyrolysis,<sup>[40]</sup> hydrothermal synthesis,<sup>[41]</sup> and electrochemical deposition.<sup>[42,43]</sup>  
6

7 Electrodeposition is low temperature (mostly <100°C) cost-effective deposition process that  
8  
9 allows the design of complex ZnO nanostructures by combining and adjusting the growth  
10  
11 conditions.<sup>[33,34,44,45]</sup> In the late 1990s, Yoshida and co-workers<sup>[46]</sup> described a one-step  
12  
13 electrodeposition of nanostructured ZnO/organic films onto conducting substrates for  
14  
15 photovoltaic applications, by adding water-soluble dyes such as tetrasulfonated  
16  
17 metallophthalocyanines to the electrochemical bath containing Zn(NO<sub>3</sub>)<sub>2</sub>. The loading of  
18  
19 organic molecules into ZnO films was also attempted using a ZnCl<sub>2</sub> bath employing cathodic  
20  
21 reduction of dissolved molecular oxygen precursor.<sup>[47,48]</sup> In the present study, electrodeposited  
22  
23 ZnO layer will be used as matrix for the incorporation of molecular catalysts.  
24  
25  
26  
27

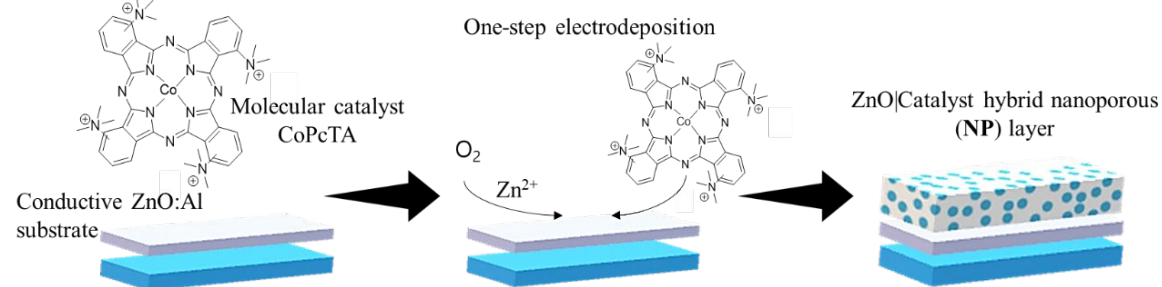
28 Incorporation of molecular catalysts onto the surfaces of electrodes can be achieved in a variety  
29  
30 of manners. Typically, grafting methods are used where the catalyst's ligand structure is  
31  
32 chemically modified with appropriate anchoring groups that allows surface binding in either  
33  
34 through a non-covalent or a covalent mode. Polymer binders can also be used to immobilize  
35  
36 catalysts on the surface of electrodes.<sup>[49]</sup> However, immobilized catalyst on the electrodes  
37  
38 surface must remain stable for long periods of time under catalytic operating conditions. In  
39  
40 addition, immobilization should not hinder the catalytic activity of the complex. Developing  
41  
42 nanostructure organic-inorganic hybrid catalysts in which a metal oxide can act as a porous  
43  
44 cage that grows around the molecular catalyst, allowing the diffusion of substrate and product  
45  
46 molecules in and out of the catalytic material, not only can prevent the catalyst from leaching  
47  
48 out, but also can provide large electrochemical surface areas, and increases CO<sub>2</sub> adsorption  
49  
50 capacity around the active sites, resulting in excellent efficiency and long-term stability in CO<sub>2</sub>  
51  
52 reduction. However, to our knowledge, very limited reports have exclusively focused on  
53  
54 implementing this strategy in the electrochemical reduction of CO<sub>2</sub>.  
55  
56  
57  
58  
59  
60

1  
2  
3 Herein, we present the preparation of molecular metal complexes-modified nanostructured zinc  
4 oxide (ZnO) thin films electrodes, focusing in the attractive ability to tune their chemical,  
5 optical, electrical, and catalytic properties by altering the film composition and thickness. The  
6 strength of the proposed method lies in its one-step electrodeposition route to produce  
7 nanoporous or nanostructured oxide matrix while simultaneously encapsulating the catalyst.  
8 Two different nanostructured electrodes with self-supported catalyst hybrid layers were  
9 developed. First, **CoPcTA**, a water-soluble tetracationic Co phthalocyanine complex, was  
10 designed to act as an encapsulated molecular catalyst within a transparent and conductive ZnO  
11 nanoporous matrix. In a two-step deposition process, the aforementioned hybrid layers were  
12 also deposited on ZnO nanorods, resulting in 3D ZnO hierarchical structures (Figure 1). Finally,  
13 the possibility of replacing **CoPcTA** with other water-soluble molecular catalysts such as tetra-  
14 sulfonated cobalt porphyrin (**CoTSPP**) or a tetra-sulfonated nickel phthalocyanine (**NiTSPc**)  
15 has been investigated, emphasizing the versatility of the preparation method, which could be  
16 used for the incorporation of a wide range of molecular complexes containing various metals  
17 and ligands. A combination of analytical, UV-vis, ICP, XPS, ATR-IR, and EDX-mapping  
18 techniques was used to confirm the incorporation and potential synergy between metal organic  
19 catalysts and the oxide matrix. Linear/cyclic voltammetry and controlled potential electrolysis  
20 (CPE) experiments confirmed the accessibility and catalytic activity of the hybrid organic-  
21 inorganic layers. Material characterization and redox behavior versus CO<sub>2</sub> reduction have been  
22 investigated, demonstrating homogeneous dispersion and control of molecular metal complex  
23 loading through the oxide matrix. These hybrid electrodes were tested as cathode material in  
24 electrocatalysis. Taking as illustrative example the CO<sub>2</sub> reduction, their remarkable potential  
25 was demonstrated.

## 58 **Results and Discussion**

**Hybrid electrodes' preparation and characterization.** In this work, electrodeposited ZnO was first used as a matrix for incorporation of CoPcTA, a water-soluble molecular Cobalt phthalocyanine catalyst. A glass covered with 350 nm of ZnO:Al layer deposited by atomic layer deposition (ALD) was used as substrate. The procedure to fabricate the nanostructured electrodes is schematically shown in Figure 1, along with microscopic characterization data (Figure 2). Two nanostructured layers have been developed and combined with a molecular catalyst: nanoporous ZnO|CoPcTA structure (NP) (Figure 1a) and 3D hierarchical structure made of 20 nm of nanoporous ZnO|CoPcTA structure (NP) grown on zinc oxide nanorods (ZNRs) (Figure 1b).

**a) Hybrid Zinc oxide|catalyst layer electrodeposition**



**b) 3D ZnO hierarchical structure electrodeposition**

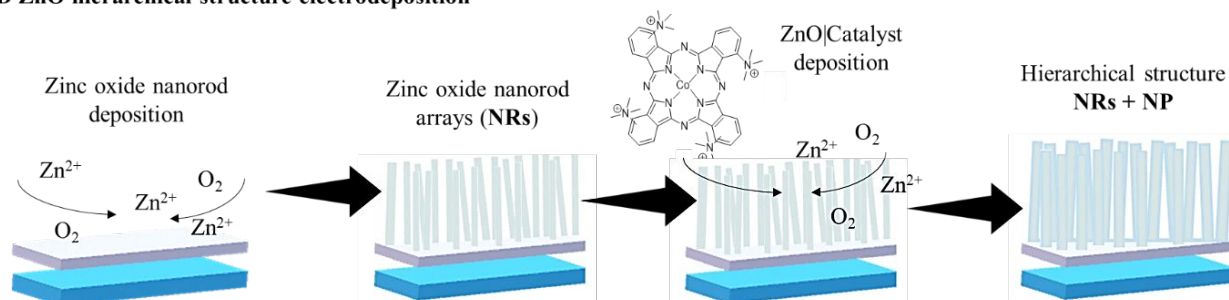


**Figure 1** Schematic representation of the preparation of the ZnO nanostructures. a) Hybrid ZnO|CoPcTA nanoporous (NP) layers, b) Hierarchical 3D structures made of zinc oxide nanorod arrays (NRs) coated by a hybrid ZnO|catalyst nanoporous (NP) layer (ZnO NRs + ZnO|CoPcTA NP).

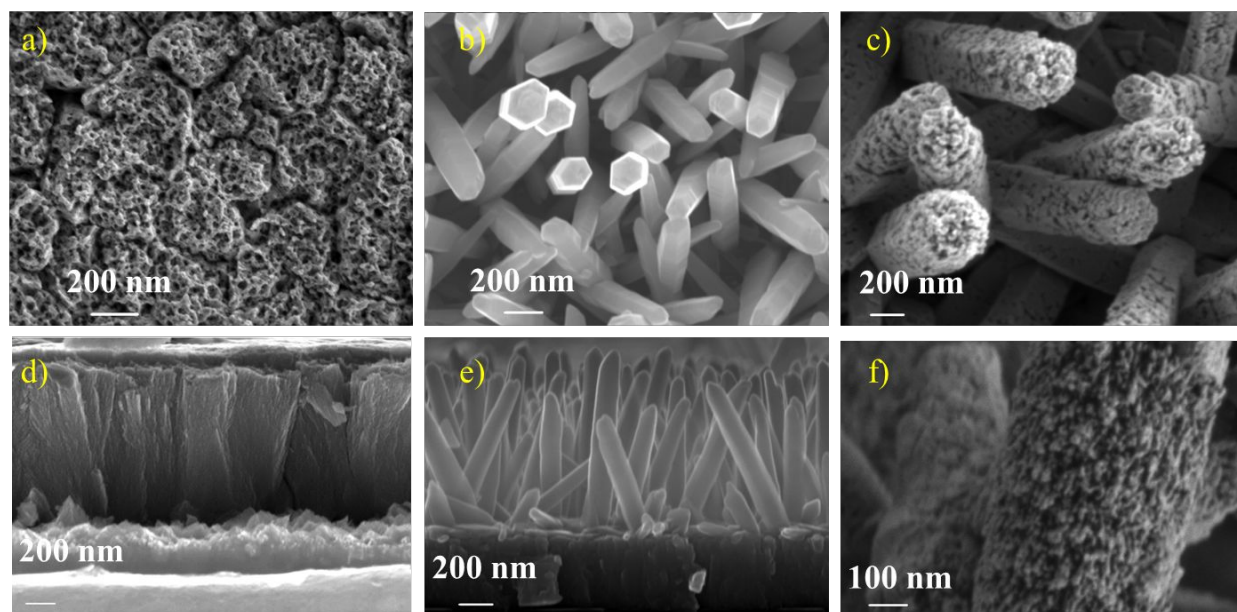


**Figure 2** Top view and cross section SEM images of the different ZnO nanostructures presented in this work: a,d) **ZnO|CoPcTA NP**, b,e) **ZnO NRs**, c,f) **ZnO NRs** covered by a thin **ZnO|CoPcTA NP** layer.

The electrodeposition of the **ZnO|CoPcTA** hybrid layers was carried out at constant potential in an aqueous oxygen saturated solution containing  $\text{ZnCl}_2$ , KCl salts and **CoPcTA** (see experimental section for details). Figure 3 compared the X-ray diffraction patterns under grazing incidence (GIXRD) of the ALD-ZnO:Al substrate with those of a **ZnO|CoPcTA NP** layer, pure **ZnO NRs**, and a hybrid 3D structure of **ZnO NRs** covered by a  $\sim 20$  nm **ZnO|CoPcTA NP** layer. For all layers, the diffraction patterns match the standard diffraction patterns of the hexagonal wurtzite ZnO crystal structure (JCPDS-36-1451).<sup>[50]</sup> ALD ZnO:Al substrate (Figure 3a) presents a mixed (100), (101) and (110) orientation indicating that the c-axis of ZnO is mostly parallel to the substrate. As observed on the SEM images (Figures 2a & 2d), addition of the molecular catalyst during the growth of ZnO seems to strongly affect the crystal growth mechanism of the ZnO, leading to a significantly higher surface area, resulting in a sponge like nanoporous structure. The comparison of the X-ray diffraction patterns of **ZnO|CoPcTA** nanoporous layer with the ALD ZnO:Al substrate show an increased peak intensity of the (002) planes for the nanoporous layer as well as appearance of (102) and (103) reflections (Figure

3c). The nanoporous film is thus mainly oriented according to the (002) reflection which corresponds to the c-axis of the wurtzite type lattice. Such preferential orientation is often observed for ZnO layers, as the (002) crystal face is the densest and the most stable thermodynamically.

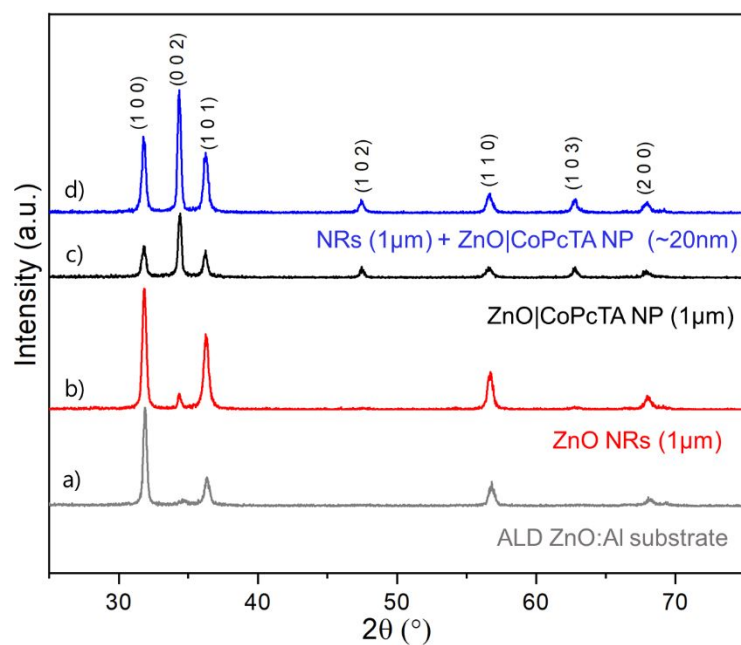


**Figure 3** GIXRD patterns under grazing incidence for: a) ALD ZnO:Al substrate, b) **ZnO NRs** 1  $\mu\text{m}$  grown on ALD ZnO:Al substrate, c) **ZnO|CoPcTA NP** layer grown on ALD ZnO:Al substrate and d) **ZnO NRs** covered by **ZnO|CoPcTA NP** layer (NRs + NP).

When **ZnO NRs** are grown on ALD ZnO:Al substrate, it results in non-vertical randomly oriented rods as observed on SEM images (Figures 2b and 2e), while presenting the same crystalline orientation and diffraction plans as the ALD-ZnO:Al substrate (Figure 3b). Interestingly when **ZnO|CoPcTA NP** layer is grown on **ZnO NRs** (Figure 3d), the same preference orientation occurs as with the **ZnO|CoPcTA NP** layer for which the most intense peak remains the (002). This confirms that, when **CoPcTA** is added to the deposition bath, whatever the substrate orientation, nanoporous layers tend to self-organize with a preferential c-axis orientation along (002) plane. For these layers, SEM pictures show a hierarchical structure composed by a hybrid **ZnO|CoPcTA NP** coat surrounding the nanorods (Figures 2c and 2f).

1  
2  
3 Effective covering of **ZnO NRs** arrays with **NP** layers has been achieved by varying the total  
4 charge transferred during the electrodeposition (Supplementary Figure S1).  
5  
6  
7  
8  
9

10 The thickness of the **ZnO|CoPcTA NP** layer can be controlled by varying the transferred  
11 charge throughout the process. Increasing the charge from 0.5 to 4 C cm<sup>-2</sup> results in a linear  
12 increase in NP layer thickness from 20 nm to 1200 nm (Supplementary Figure S2). It has been  
13 shown that, adding a water-soluble molecular complex to the ZnO electrodeposition bath can  
14 not only act as a structure directing agent but also results in its incorporation inside the  
15 nanoporous ZnO layer.<sup>[44,47]</sup> Inductively coupled plasma optical emission spectrometry (ICP–  
16 OES) and optical absorption measurements on **ZnO|CoPcTA NP** samples were performed to  
17 confirm the incorporation of the molecular catalyst into the electrodeposited layers  
18 (Supplementary Figure S3). The results of ICP measurements are presented in Figure 4b, showing  
19 that after dissolution of the layers (acidic treatment with water diluted nitric acid), catalyst  
20 loadings ranged from 0.8 ± 0.2 nmol cm<sup>-2</sup> for a **ZnO|CoPcTA NP** layer 50 nm thick, up to 7.8  
21 ± 0.7 nmol cm<sup>-2</sup> for **ZnO|CoPcTA NP layer** 1 μm thick. The concentration of the **CoPcTA**  
22 molecule in the layers is linearly correlated to the film thickness. Furthermore, the optical  
23 absorbance measurements show that the **ZnO|CoPcTA NP** samples present an absorbance peak,  
24 around 665 nm, in a wavelength range which is close to the absorbance peak of **CoPcTA**  
25 molecule in aqueous solution (Figure 4a). A linear relationship is observed between layer  
26 thickness and the **CoPcTA** concentration inside the layer (Supplementary Figure S4), as well  
27 as between the layer thickness and the absorbance at 665 nm (Figure 4b). This strongly suggests  
28 the molecule's incorporation into the hybrid layers, the amounts of which can be adjusted by  
29 controlling the deposition time (i.e. the charge transferred).  
30  
31  
32  
33  
34  
35  
36  
37  
38  
39  
40  
41  
42  
43  
44  
45  
46  
47  
48  
49  
50  
51  
52  
53  
54  
55  
56  
57  
58  
59  
60

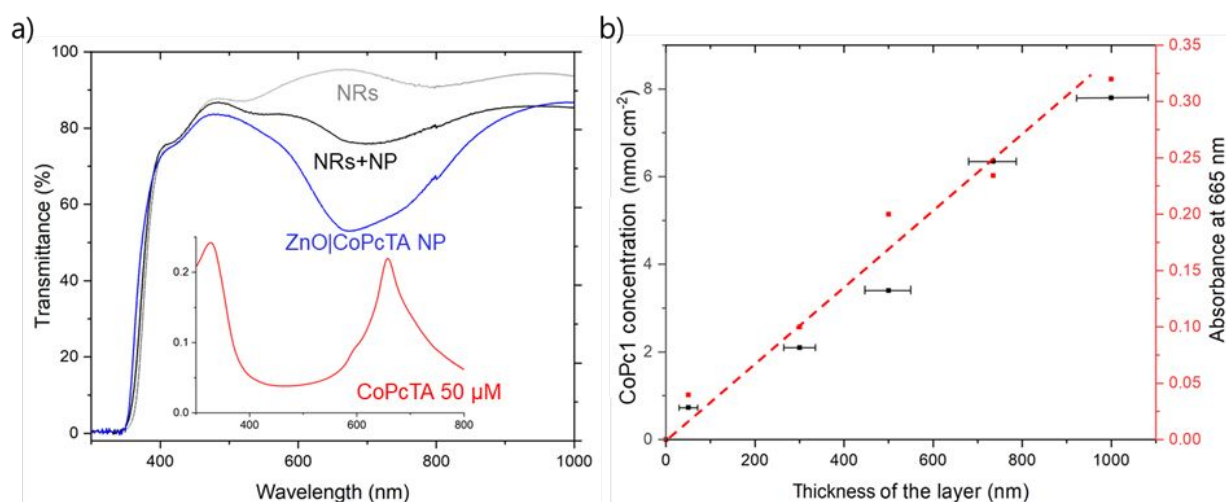


**Figure 4** a) Optical transmission of electrodeposited **ZnO NRs** (1  $\mu\text{m}$ , grey), **ZnO|CoPcTA NP** layer (1  $\mu\text{m}$ , blue) and 3D **ZnO NRs** (1  $\mu\text{m}$ ) coated by a **ZnO|CoPcTA NP** (20 nm, black), on ALD-ZnO:Al. Inset: Absorbance of the **CoPcTA** molecule in aqueous solution (concentration = 50  $\mu\text{M}$ , red). b) Concentration of **CoPcTA** molecules in the **ZnO NP** layers measured by ICP as a function of the thickness of the layer and comparison to the absorbance of the same samples at  $\lambda = 665$  nm.

The incorporation of molecular catalysis in **ZnO|CoPcTA NP** being confirmed, ICP analysis were performed on a 3D **ZnO NRs** (1  $\mu\text{m}$ ) covered with 20 nm of **ZnO|CoPcTA NP** layer. In these layers, the ICP analysis shows a **CoPcTA** concentration around 0.73  $\text{nmol cm}^{-2}$ , which corresponds to approximately ten times less than the one measured for a 1  $\mu\text{m}$  thick **ZnO|CoPcTA NP** layer.

Figure 3a compared optical transmission of electrodeposited **ZnO NRs** (1  $\mu\text{m}$ ), **ZnO|CoPcTA NP** layer (1  $\mu\text{m}$ ) and 3D **ZnO NRs** (1  $\mu\text{m}$ ) coated by a **ZnO|CoPcTA NP** (20 nm), on ALD-ZnO:Al substrate and the absorbance of an aqueous solution of the pure **CoPcTA** molecule (50  $\mu\text{M}$ ). In the visible range, the transparency of **ZnO NRs** approaches 90%. The impact on the total transmission of the incorporation of the **CoPcTA** molecule into the nanoporous **ZnO|CoPcTA NP** layers becomes clear between 525 and 1000 nm, with a decrease from  $\sim 97\%$  transmission to  $\sim 55\%$  (580 to 700 nm range) for a 1  $\mu\text{m}$  thick **ZnO|CoPcTA NP** layer. Such

decrease originates from Co complex incorporation, **CoPcTA** presenting an absorption peak around 665 nm. Optical transmission is significantly improved (>75%) upon using hierarchical structure **ZnO NRs+NP** thanks to the very low amount of catalyst incorporated in the structure.

Dispersion and distribution of the catalyst into the nanoporous layers was also investigated by EDX-mapping measurement. Images from a 1  $\mu\text{m}$  thick **ZnO|CoPcTA NP** electrode (Supplementary Figure S5) show signals from the O, Zn, Cl atoms of the ZnO matrix, but also signals from Co, definitively confirming the catalyst incorporation into the film during the electrodeposition. Additionally, mapping of Co element revealed the absence of cobalt aggregates, suggesting a homogeneous distribution of the catalyst in the oxide material.

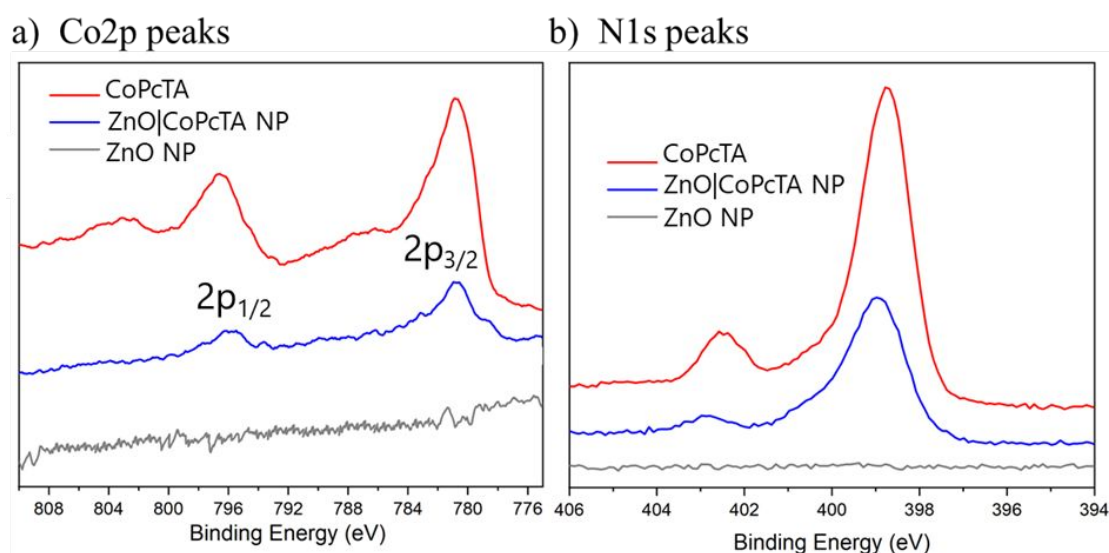


**Figure 5** Comparison of the XPS core level spectra of (a) Co 2p, (b) N 1s for: **CoPcTA** molecule, **ZnO|CoPcTA NP** electrode and a blank ZnO electrode.

XPS measurements were performed to assess the presence of the **CoPcTA** molecule and its eventual interaction with the electrodeposited ZnO matrix. The Co 2p and N 1s signals obtained for **CoPcTA**, **ZnO|CoPcTA NP**, and a blank ZnO layer with no molecular complex are compared in Figure 5. From **ZnO|CoPcTA NP**, two peaks corresponding to Co 2p signals indicative of a  $\text{Co}^{2+}$  oxidation state are observed (Figure 5a), with a main peak ( $2p_{3/2}$ ) at 780 eV

1  
2  
3 and a secondary peak at ( $2p_{1/2}$ ) at 796 eV.<sup>[51]</sup> In Figure 5b, signals from nitrogen were also  
4 detected on the surface of the **ZnO|CoPcTA NP** electrodes, with N1s signal peak at 398.8 eV,  
5 a similar value to the characteristic binding energy of the isoindolic N in phthalocyanines  
6 complexing a cobalt atom (BE = 399.3 eV).<sup>[51]</sup> This peak reflects the configuration of the  $\text{CoN}_4$   
7 centre with four equivalent nitrogen atoms coordinating a  $\text{Co}^{2+}$  ion. Furthermore, a small  
8 additional N1s peak centred at 402.5 eV is observed, which is typically assigned to N–O  
9 bonds,<sup>[52]</sup> indicative of a possible interaction between the N atoms of the **CoPcTA** molecule  
10 and of the oxygen atoms of the sample holder (Si wafer covered by native oxide). All these  
11 results clearly confirm that **CoPcTA** is incorporated into the hybrid **ZnO|CoPcTA NP** layer.  
12  
13 In order to have a better understanding of the interactions between the molecular catalyst and  
14 the inorganic ZnO matrix, the O 1s and Zn 2p XPS spectra of **ZnO|CoPcTA NP** layers were  
15 also compared to the blank ZnO layers (Supplementary Figure S6). Observed peaks do not  
16 show any shift in the binding energy value before and after the incorporation of the molecular  
17 catalyst. However, further analysis must be done in the future to probe for the possible  
18 interactions between the molecule and the ZnO inorganic matrix.

19  
20  
21  
22  
23  
24  
25  
26  
27  
28  
29  
30  
31  
32  
33  
34  
35  
36  
37  
38 The infrared spectroscopy analysis (ATR-IR) of **CoPcTA**, of a 1  $\mu\text{m}$  **ZnO|CoPcTA NP** sample  
39 and of a ZnO blank sample were also compared (Supplementary Figures S7). The analysis data  
40 revealed similar fingerprint regions between **CoPcTA** powder and **CoPcTA** loaded into the  
41 **ZnO|CoPcTA NP** layer, which further evidences that the catalyst is well entrapped into the  
42 ZnO electrodeposited layer. The metal to ligand (M–N) vibration of **CoPcTA** could be observed  
43 at  $910\text{ cm}^{-1}$ , as well as peaks around  $1080\text{ cm}^{-1}$  (C–N stretching bending vibrations) and at  $1393$   
44  $\text{cm}^{-1}$ . These latter are assigned to aromatic ring stretching vibrations, showing a perfect match  
45 with the vibration obtained with a **CoPcTA** powder sample. The peaks from the  $\text{CH}_3$  groups at  
46  $2895$  and  $2986\text{ cm}^{-1}$  indicate structural preservation of the organic molecule upon incorporation  
47 into the ZnO inorganic matrix.<sup>[53]</sup>

1  
2  
3 **Electrochemical CO<sub>2</sub> reduction by ZnO|catalyst hybrid nanostructures.** The catalytic  
4 activity of the **ZnO|CoPcTA NP** electrodes was first explored by cyclic voltammetry (CV) in  
5 an acetonitrile solution containing 0.6 M H<sub>2</sub>O and 0.1 M tetrabutylammonium  
6 hexafluorophosphate (TBAPF<sub>6</sub>). A catalytic current with an onset potential at ca. -1.6 V vs.  
7 SCE was observed when the solution was saturated with CO<sub>2</sub> (Figure 6a). Addition of H<sub>2</sub>O as  
8 proton source (0.33 M, 0.44 M and 0.67 M respectively) was investigated. As observed in the  
9 cyclic voltammograms (Supplementary Figure S8a), H<sub>2</sub>O concentration increase resulted in an  
10 enhancement of the current density and in a decrease of the overpotential of ca. 200 mV upon  
11 going from 0.33 to 0.67 M H<sub>2</sub>O. Adding more water (> 0.7 M) did not show a significant impact  
12 on the current density, but accelerated the degradation of the electrodes. Furthermore,  
13 increasing the thickness of the NP layers allows to reach higher current densities, as quantified  
14 by CVs of 50 nm, 530 and 1000 nm thick **ZnO|CoPcTA NP** layers that displayed c.a. 0.5, 1.4  
15 and 2.0 mA cm<sup>-2</sup> respectively (Supplementary Figure S8b). The increase of the current density  
16 with the thickness of the NP layer suggests that the current density depends on the active surface  
17 area of the electrodes as well as the amount of catalyst inserted into the layers. Thanks to the  
18 nanoporous structure of the electrodes, the reactant CO<sub>2</sub> can access to the active sites even in a  
19 1 μm thick layer.  
20  
21  
22  
23  
24  
25  
26  
27  
28  
29  
30  
31  
32  
33  
34  
35  
36  
37  
38  
39  
40  
41

42 This was confirmed upon performing CPE experiments. A comparison of electrodes covered  
43 with a **ZnO|CoPcTA NP** layers of 50 ± 10 nm, 530 ± 50 nm and 1000 ± 70 nm thickness  
44 respectively (Supplementary Figure S9) showed current density increase with the thickness of  
45 the NP layer. Even with 1 μm thick layer, the **CoPcTA** molecules incorporated into the ZnO  
46 nanoporous matrix are accessible and can react with CO<sub>2</sub>, the electrocatalytic overall process is  
47 only partially limited by diffusion of the reactant and charge transport through the oxide film.  
48 Moreover, these results add further evidence that the **CoPcTA** catalyst is well dispersed and  
49 distributed throughout the thickness of the layer and not just on the surface. The electrodes  
50 showed a good stability for 45 minutes CPE. During the first 10 minutes, the current gradually  
51  
52  
53  
54  
55  
56  
57  
58  
59  
60

increased until it reached a steady-state value staying stable until the end of the experiment. This behavior may be due to the porosity of our layers, since it takes some time for the reactant ( $\text{CO}_2$ ) to fill and reach all the porosity of the layer; in addition, similar time effect may also impact the progressive charging of the film (charge transport to the catalytic sites).

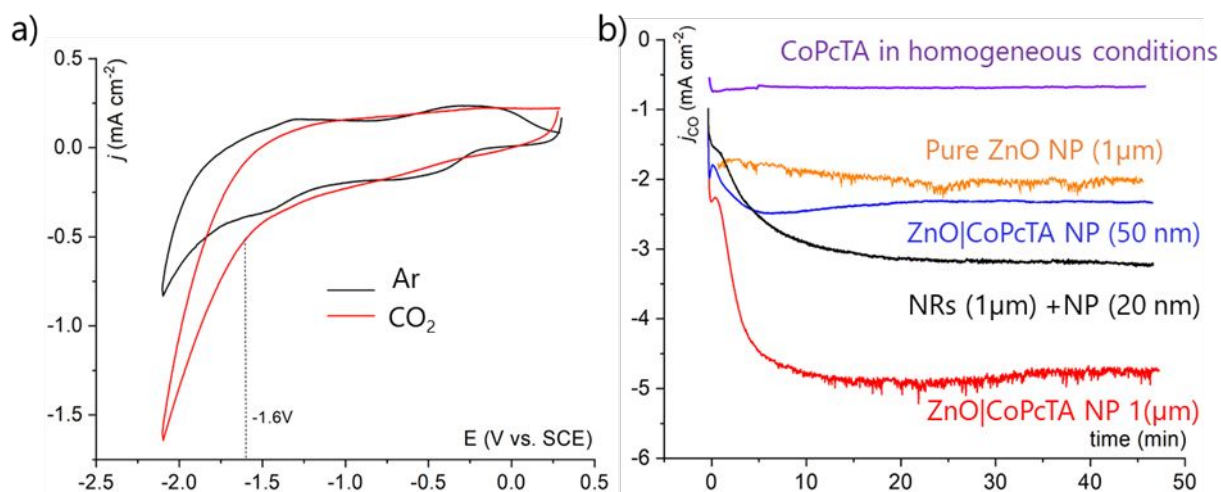


**Figure 6** (a) Cyclic voltammograms recorded in Ar (black) and  $\text{CO}_2$  (red) saturated acetonitrile solution + 0.1 M  $\text{TBAPF}_6$  at a 1  $\mu\text{m}$  thick **ZnO|CoPcTA NP** electrode. Electrode surface 0.5  $\text{cm}^2$ , scan rate 0.1  $\text{V s}^{-1}$ . (b) CPE at  $E = -2.1 \text{ V vs. SCE}$  in a  $\text{CO}_2$  saturated acetonitrile solution + 0.1 M  $\text{TBAPF}_6$  and 0.67 M  $\text{H}_2\text{O}$  for: **CoPcTA** (0.5 mM) in homogeneous conditions (purple), a 1  $\mu\text{m}$  thick ZnO porous layer without catalyst (orange), a  $50 \pm 10 \text{ nm}$  thick **ZnO|CoPcTA NP** layer (blue), a 1  $\mu\text{m}$  thick **ZnO NRs** covered by a 20 nm thick **ZnO|CoPcTA NP (NRs+NP)** layer (black) and a  $1000 \pm 70 \text{ nm}$  thick **ZnO|CoPcTA NP** layer (red).

CPE experiments at  $E = -2.1 \text{ V vs. SCE}$  (45 min duration) were performed with all electrode structures and are compared in Figure 6b. First, the **CoPcTA** molecule in homogeneous conditions showed a weak catalytic activity with a current density of  $-0.45 \text{ mA cm}^{-2}$ , while gas chromatography (GC) analysis of the products indicated formation of CO with 60.8 % selectivity (Table 1, entry 1). A ZnO nanoporous layer can reduce  $\text{CO}_2$  to CO with 73.7 % selectivity at  $j = -2 \text{ mA cm}^{-2}$  (Table 1, entry 2), i.e. a partial current density for CO production  $j_{\text{CO}} = -1.5 \text{ mA cm}^{-2}$ , confirming catalytic activity of the ZnO itself to reduce  $\text{CO}_2$  to CO, as reported previously.<sup>[29,32,53–58]</sup> When both components, **CoPcTA** complex and ZnO are

1  
2  
3 combined in a hybrid material, significant enhancement of the CO<sub>2</sub> reduction reaction is  
4 obtained. CPE experiments using **ZnO|CoPcTA NP** layers led to typical current density  
5 ranging from -2.45 mA cm<sup>-2</sup> up to -5 mA cm<sup>-2</sup> (i.e. ranging from  $j_{CO} = 2.4$  mA cm<sup>-2</sup> to  $j_{CO} =$   
6 4.95 mA cm<sup>-2</sup> respectively), when layer thickness increases from 50 to 1000 nm respectively,  
7 while producing CO with selectivity above 97 % (Table 1, entries 3-5). The presence of a small  
8 amount of **CoPcTA** into the layers induces not only an important increase of the current density  
9 but also strongly improves the selectivity of the reaction. These results illustrate the synergetic  
10 effect of the cobalt complexes and zinc oxide for boosting the catalysis, possibly occurring from  
11 the joint coordination of CO<sub>2</sub> molecules at the cobalt sites along with assistance from the zinc  
12 ions (Lewis acid sites) which provide stabilisation of the partial negative charge developing on  
13 the oxygen atoms of the CO<sub>2</sub> and weakening of the C-O bonds. Remarkably, turnover number  
14 (TON) as high as 17,885 and turnover frequency (TOF) of 9.4 s<sup>-1</sup> were obtained for the thin (50  
15 nm) NP layer (Table 1, entry 3), standing among the highest performance so far obtained for an  
16 immobilised metal complex electrocatalyst.<sup>[6,10,59]</sup> TOF value decrease slightly when the  
17 thickness of the layer increases (Table 1, compare entries 3, 4 and 5), meaning that an overall  
18 faster catalysis occurs in a thin layer compare with a thick layer, which may be due to  
19 progressive growing influence of charge transport and diffusional effect limitation in the thicker  
20 layers, even if the current density increases across the series of electrodes.  
21  
22  
23  
24  
25  
26  
27  
28  
29  
30  
31  
32  
33  
34  
35  
36  
37  
38  
39  
40  
41  
42  
43  
44  
45

46 Comparison of CPE experiments of an electrode with a 50 nm **ZnO|CoPcTA NP** thin layer  
47 (Figure 6b, blue) with a 3D nanostructured electrode (**NRs** 1 μm covered by a **ZnO|CoPcTA**  
48 **NP** 20 nm, Figure 6b, black line), both incorporating a similar amount of molecular catalyst  
49 (0.85 nmol cm<sup>-2</sup> and 0.73 nmol cm<sup>-2</sup> respectively), showed an enhancement of the catalytic  
50 performance towards the CO<sub>2</sub>RR for the 3D structure. The partial current density  $j_{CO}$  reached  
51 by the NP thin layer for CO production is ca. -2.4 mA cm<sup>-2</sup> whereas the 3D structured electrode  
52 achieved an absolute higher ( $j_{CO} = -2.8$  mA cm<sup>-2</sup>) current density. The 3D structured electrode  
53  
54  
55  
56  
57  
58  
59  
60

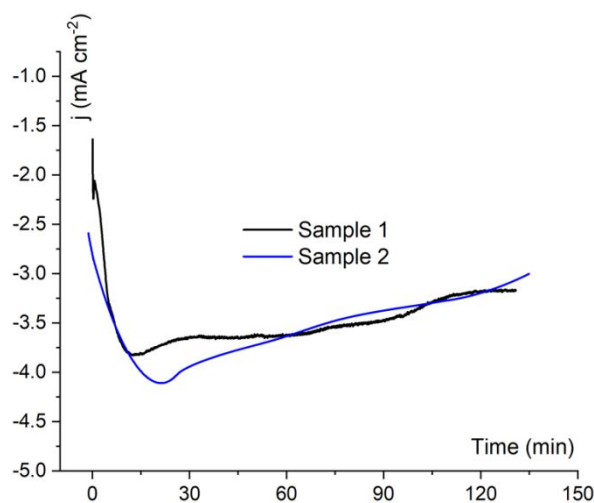
also furnished a higher TOF of  $11.7 \text{ s}^{-1}$  (Table 1, compare entries 3 and 7), meaning that the CO production goes fast in the 3D nanostructured electrodes. Combination of good electronic transport properties and the high exposed surface of the **ZnO NRs** with the catalytic hybrid layer results in an enhancement of the catalytic performance towards the  $\text{CO}_2\text{RR}$ .

**Table 1.** Comparative data of performance of the different ZnO nanostructures catalytic materials during a 45 minute electrolysis experiment at a constant potential  $E = -2.1 \text{ V vs. SCE}$  in  $\text{CO}_2$ -saturated acetonitrile solution containing  $0.1 \text{ M TBAPF}_6$  and  $0.67 \text{ M H}_2\text{O}$ . Electrode surface =  $1 \text{ cm}^2$ .

Entry	Sample	Catalyst amount	Current density ( $\text{mA cm}^{-2}$ )	Total FE (%)	Selectivity		TON	TOF ( $\text{s}^{-1}$ )
					%CO	%H <sub>2</sub>		
1	CoPcTA in homogeneous solution	0.5 mM	-0.45	98.1	60.8	39.2	0.93	0.001
2	Blank ZnO nanoporous layer 1000 nm	0	-2.04	99.0	73.7	26.3	-	-
3	ZnO CoPcTA NP $50 \pm 10 \text{ nm}$	0.81 nmol	-2.45	98.6	97.4	2.6	17885	9.4
4	ZnO CoPcTA NP $500 \pm 50 \text{ nm}$	1.86 nmol	-3.37	99.6	98.4	1.6	9283	4.9
5	ZnO CoPcTA NP $1000 \pm 70 \text{ nm}$	2.80 nmol	-5.0	97.1	98.9	1.1	8280	4.4
6	ZnO NRs $1 \mu\text{m}$	0	0.9	98.0	73.5	26.5	-	-
7	ZnO NRs $1 \mu\text{m}$ + ZnO CoPcTA NP $20 \text{ nm}$	0.75 nmol	-2.9	91.0	96.7	3.3	22242	11.7

We investigated the stability of the electrodes upon performing long-term CPE at  $-2.1 \text{ V vs. SCE}$  (2 h) using two samples ZnO|CoPcTA NP layers  $750 \pm 50 \text{ nm}$  thick (Figure 7). Average catalytic current of  $3.5 \text{ mA cm}^{-2}$  were obtained. Gas chromatography analysis of the products indicated the formation of CO with ca. 97% FE along with  $\text{H}_2$  as only by-product (3%), giving a complete Faradaic efficiency. The current density, after reaching a steady-state value in the first 5 min, remained stable along the electrolysis with only a slight decay. ICP analysis of the electrode before and after 2 h of electrolysis revealed a 10% loss of the catalyst from the electrode to the solution. This decrease may reflect partial cathodic reduction of the ZnO into metallic Zn, which could further lead to some catalyst leak. To verify this hypothesis, XPS analyses were performed to characterize the surface properties of the samples before and after

1  
2  
3 CPE. Due to the comparable binding energies of Zn and ZnO in the Zn 2p region of the XPS  
4 spectrum, we compared the Zn LMM Auger peaks of the as-prepared and used **ZnO|CoPcTA**  
5 **NP** samples. As shown in Fig S10a, both samples exhibited the typical Auger peaks of ZnO,  
6 with a main peak at ~499 eV and a shoulder at ~496 eV. Notably, no Zn peaks are present after  
7 CPE. However, XRD measurements of the **ZnO|CoPcTA NP** sample after CPE (figure S10b)  
8 showed the presence of diffraction peaks from Zn at  $2\theta = 43.1^\circ$  and  $54.2^\circ$  corresponding to the  
9 (101) and (102) lattice planes of hexagonal phase from Zn metal respectively,<sup>[60]</sup> indicating that  
10 a fraction of the oxidized Zn species were reduced to metallic Zn during electrolysis. Part of  
11 the layer may thus have been dissolved which could explain the loss of the catalyst. Overall,  
12 the above results indicate that the **ZnO|Catalyst** films are quite stable with catalytic activity  
13 being sustained for hours.



14  
15  
16  
17  
18  
19  
20  
21  
22  
23  
24  
25  
26  
27  
28  
29  
30  
31  
32  
33  
34  
35  
36  
37  
38  
39  
40  
41  
42  
43  
44  
45  
46  
47  
48  
49  
50  
51  
52  
53  
54  
55  
56  
57  
58  
59  
60  
**Figure 7** CPE at  $E = -2.1$  V vs. SCE in a  $\text{CO}_2$  saturated acetonitrile solution + 0.1 M  $\text{TBAPF}_6$  and 0.67 M  $\text{H}_2\text{O}$  for two  $750 \pm 50$  nm **ZnO|CoPcTA NP** layer electrodes.

In addition to the **ZnO|CoPcTA NP** layers, a porphyrin Cobalt complex (**CoTSPp**) and a Nickel phthalocyanine complex (**NiTSPc**), both bearing four sulphonated groups, were used to grow ZnO nanoporous layers **ZnO|CoTSPp NP** and **ZnO|NiTSPc NP**. CPE experiments were performed with these electrodes of similar thickness and compared with those investigated

1  
2  
3 before. Total current density of -1.85, -1.75 and -1.7 mA cm<sup>-2</sup> were respectively obtained for  
4  
5 **ZnO|CoPcTA NP**, **ZnO|CoTSPP** and **ZnO|NiTSPc NP** electrodes (Supplementary Figure  
6  
7 S11). They showed very similar selectivity for CO production, 93.3%, 96.9%, and 96.8%  
8  
9 respectively (Supplementary Table S1).

10  
11  
12 The electroreduction of CO<sub>2</sub> exemplified in the above described examples illustrate the  
13  
14 versatility of the preparation method that could be used for the incorporation of a variety of  
15  
16 molecular complexes with different metal and ligands with a systematic positive impact of the  
17  
18 metal oxide matrix, thus opening a wide range of possibilities for performing various  
19  
20 electrocatalytic reactions.  
21  
22  
23  
24  
25

## 26 **Conclusions**

27  
28 Hybrid ZnO|catalyst films have been electrodeposited on transparent conductive electrodes by  
29  
30 a simple one-step method. The grown nanostructured oxide layers are highly porous and can be  
31  
32 loaded with water soluble metal (e.g Co, Ni) complexes during the electrodeposition process.  
33  
34 Both the thickness (from a few tens of nm to a μm) and nanostructuring (2D, 3D hierarchical  
35  
36 structures) of the oxide layers can be controlled, as well as the quantity of encapsulated  
37  
38 molecular complexes, which appear to be homogeneously dispersed in the films. These films  
39  
40 are electrochemically active thanks to high porosity and conductivity. Such modified electrodes  
41  
42 may be used for various applications in electrochemical devices. As an illustrative example,  
43  
44 selective and fast electroreduction of CO<sub>2</sub> to CO has been achieved, showing synergetic effect  
45  
46 between the molecular catalyst and the zinc oxide hosting matrix. Such approach could now be  
47  
48 applied to other electrocatalytic processes. Remarkably, these electrodes also present a  
49  
50 significant visible light transmission, which may enable their use as a front contact in  
51  
52 photovoltaics and photocatalytic devices. This opens up for a modular approach where the  
53  
54 photo-absorber and the molecular-catalysts can be developed, tested, optimized, and exchanged  
55  
56 independently.  
57  
58  
59  
60

## Methods

**Catalyst synthesis.** Reagents were purchased from Aldrich and used without further purification. 3-(dimethylamino)phthalonitrile was synthesized according to literature.<sup>[10]</sup> (See catalyst synthesis characterizations in Supplementary). Tetra-sulfonated cobalt porphyrin **CoTSP** and tetra-sulfonated nickel phthalocyanine **NiTSPc** were purchased from Aldrich.

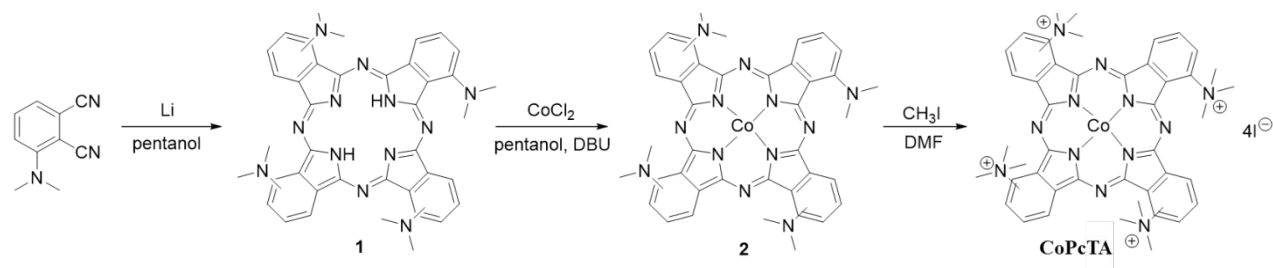


**Figure 8.** Synthetic route for CoPcTA

*Synthesis of phthalocyanine 1.* Granules of lithium were added to anhydrous n-pentanol (10 mL). This mixture was heated to 60 °C under argon flux until total consumption of the granules. 3-(dimethylamino)phthalonitrile (0.5 g, 2.92 mmol) was added and this reaction mixture was refluxed for 18 h. It was then cooled to room temperature and poured into an ethanol/water mixture. The resulting precipitate was filtered off, washed several times with water and dried. Phthalocyanine **1** (Figure 8) was obtained by chromatography on silica gel using a mixture of CH<sub>2</sub>Cl<sub>2</sub>/EtOH (20:1) as the eluent. Yield: 35% (175 mg). FT-IR ( $\nu$ , cm<sup>-1</sup>): 3290, 3073, 2944, 2832, 2775, 1576, 1485, 1433, 1321, 1186, 1135, 1083, 1035, 970, 879, 804, 745, 667. <sup>1</sup>H NMR (500 MHz, DMSO-d<sub>6</sub>):  $\delta$ , ppm, 3.64 (m, 24H), 7.45-8.10 (m, 8H), 8.87 (m, 4H). ESI-HRMS:  $m/z$  687.33840 [M]<sup>+</sup> calculated for C<sub>40</sub>H<sub>38</sub>N<sub>12</sub>: 686.8280. UV-vis (DMSO):  $\lambda_{\text{max}}$  nm (log  $\epsilon$ ) 342 (4.70), 712 (4.78), 779 (4.89).

*Synthesis of phthalocyanine 2.* Phthalocyanine **1** (165 mg, 0.24 mmol), CoCl<sub>2</sub> (72 mg, 0.48 mmol), and DBU (1 mL) in dried n-pentanol (10 mL) was heated to reflux for 18 h under argon.

1  
2  
3 After cooling to room temperature, the reaction mixture was poured into an ethanol/water  
4 mixture. The resulting precipitate was filtered off and washed several times with water.  
5  
6 Phthalocyanine **2** was purified by chromatography on silica gel using a mixture of  
7  
8 CH<sub>2</sub>Cl<sub>2</sub>/EtOH (10:1) as the eluent. Yield: 70% (125 mg). FT-IR (ν, cm<sup>-1</sup>): 3069, 2926, 2827,  
9  
10 2775, 1571, 1490, 1438, 1316, 1186, 1156, 1126, 1091, 1052, 987, 914, 870, 805, 740. ESI-  
11  
12 HRMS: m/z 744.2588 [M]<sup>+</sup> calculated for C<sub>40</sub>H<sub>36</sub>CoN<sub>12</sub>: 743.7452. UV-vis (DMSO): λ<sub>max</sub> nm  
13  
14 (log ε) 331 (4.57), 733 (4.68).  
15  
16  
17  
18  
19  
20

21 *Synthesis of phthalocyanine CoPcTA.* Phthalocyanine **2** (150 mg, 0.20 mmol) was dissolved in  
22  
23 DMF (10 mL), and methyl iodide (0.9 mL, 15 mmol) was added. The mixture was stirred at 45  
24  
25 °C for 16 h then poured into diethyl ether (25 mL). The resulting precipitate was filtered off,  
26  
27 washed with ether and hexane. Yield: 90% (145 mg). FT-IR (ν, cm<sup>-1</sup>) 3056, 3013, 2952, 2874,  
28  
29 2835, 2784, 1610, 1519, 1481, 1399, 1316, 1270, 1117, 996, 944, 805, 745. ESI-HRMS: m/z  
30  
31 804.3805 [M+H]<sup>+</sup> calculated for C<sub>44</sub>H<sub>48</sub>CoN<sub>12</sub>: 803.8852. UV-vis (DMSO): λ<sub>max</sub> nm (log ε) 330  
32  
33 (4.20), 702 (4.23).  
34  
35  
36

37 Caution/important note: in order to destroy the excess of methyl iodide, the ether filtrate is  
38  
39 treated with triethylamine.  
40  
41  
42  
43

44 *Substrate preparation.* Glass substrates (2 mm thick) covered by a transparent conductive zinc  
45  
46 oxide aluminum doped (ZnO:Al) layer of 380 nm thick were used as working electrode for all  
47  
48 the depositions. This ZnO:Al layer was deposited by Atomic Layer Deposition (ALD)  
49  
50 according to reported procedure (sheet resistance from 20.1 to 28.2 × 10<sup>-3</sup> Ω/sq).<sup>[61]</sup> The ZnO:Al  
51  
52 coated glass substrates were ultrasonically sequentially cleaned in acetone, 2-propanol, and  
53  
54 water, each for 5 min. They were activated in a KOH solution (pH 10.5) for 2 min and finally  
55  
56 rinsed with distilled water prior to electrodeposition.  
57  
58  
59  
60

1  
2  
3 **Preparation of the hybrid nanoporous catalytic layers (ZnO|cat NP).** All oxide layers were  
4 electrodeposited using a classical three electrodes setup. The reference electrode was a saturated  
5 calomel electrode (SCE) (Hach) with a potential of +0.244 V vs. NHE at 25 °C. The counter  
6 electrode was a platinum wire and the working electrodes were the mentioned ZnO:Al coated  
7 glass substrates. The electrodeposition of the zinc oxide|catalyst nanoporous hybrid layers was  
8 carried out at constant potential  $E = -1.0$  V vs SCE in an aqueous solution containing 5.0 mM  
9 ZnCl<sub>2</sub> (Sigma Aldrich >99.9%), 0.1 M KCl (ACS Reagent 99.0 – 100%) and 50 μM of the  
10 water-soluble catalyst (Cobalt phthalocyanine **CoPcTA**, tetra-sulfonated cobalt porphyrin  
11 **CoTSPP** or tetra-sulfonated nickel phthalocyanine **NiTSPc**). Oxygen gas was bubbled for 20  
12 min prior to the deposition and the same gas flow was maintained during the whole deposition  
13 processes. Temperature was maintained at 70 °C. The thickness of the layers was controlled  
14 from few tens of nm to a micrometer by varying the transferred charge. The deposited films  
15 were rinsed with water, dried in air at 100 °C for 30 min, then stored at room temperature.  
16  
17  
18  
19  
20  
21  
22  
23  
24  
25  
26  
27  
28  
29  
30  
31  
32  
33

34  
35 **Preparation of the 3D hierarchical catalytic structures (ZnO NR + ZnO|cat NP).** ZnO  
36 nanowire films were first prepared by electrodeposition on a ALD-ZnO:Al substrate, according  
37 to a method reported elsewhere.<sup>[33,34]</sup> The ZnO nanowire array layer was grown at 80 °C from  
38 a 0.2 mM ZnCl<sub>2</sub> and 0.1 M KCl solution saturated with O<sub>2</sub> by bubbling. (**ZnO NR**). The  
39 deposition process was stopped when the total transferred charge was 10 C cm<sup>-2</sup>. The deposited  
40 films were rinsed with water and dried in air at 100 °C. These electrodes were then used for the  
41 deposition of the metal oxide|catalyst hybrid layers performed as described above, leading to a  
42 structure composed of zinc oxide nanorods surrounded by a nanoporous metal oxide/catalyst  
43 layer.  
44  
45  
46  
47  
48  
49  
50  
51  
52  
53  
54  
55  
56  
57

58 **Electrochemical experiments.** Cyclic voltammetry measurements (CVs) and Controlled  
59 potential electrolysis (CPE) were performed using a PARSTAT 4000A potentiostat (Princeton  
60

1  
2  
3 Applied Research). The electrolyte was an acetonitrile solution with 0.1 M  
4 tetrabutylammonium hexafluorophosphate (TBAPF<sub>6</sub>) (98%, Aldrich), and it was saturated with  
5 argon or CO<sub>2</sub> depending on the experiment. Electrodes with hybrid catalytic layers were  
6  
7  
8  
9  
10 connected with a clip protected by PTFE tape, and the electrical contact was ensured by using  
11  
12 Gallium–Indium eutectic (Sigma Aldrich > 99.9%) covered with a copper tape. Copper was  
13  
14 isolated from the electrolyte by the PTFE tape leaving an expose surface of 0.5 cm<sup>2</sup>. The  
15  
16 mentioned before reference electrode (SCE) was immersed in the same electrolyte in a  
17  
18 separated compartment and positioned as close as possible from the working electrode. The  
19  
20 counter electrode (platinum wire or mesh) is immersed in the same electrolyte but separated by  
21  
22 a glass frit bridge.  
23  
24

25  
26 The gases used were bought from Air Liquide. Electrolysis using CO<sub>2</sub> as the substrate were  
27  
28 performed under 1 atmosphere of the gas, resulting in a concentration  $314 \pm 6$  mM at 25°C.<sup>[62]</sup>  
29  
30 The electrolysis experiments are performed in a sealed cell.  
31  
32

33  
34  
35 **Products analysis.** Gas chromatography analyses of the gases produced during electrolysis  
36  
37 were performed with an Agilent Technologies 7820A GC system equipped with a thermal  
38  
39 conductivity detector (TCD). CO and H<sub>2</sub> production were quantitatively detected and separated  
40  
41 with a CP-CarboPlot P7 capillary column (27.46 m in length and 25 μm internal diameter).  
42  
43 Temperature was held to 150 °C for the detector and 34 °C for the oven. The carrier gas was  
44  
45 argon flowing at 9.5 mL.min<sup>-1</sup> at a constant pressure of 0.5 bar. The injections were performed  
46  
47 with a 250 μL gas-tight (Hamilton) syringe. These conditions allow simultaneous detection of  
48  
49 both H<sub>2</sub>, O<sub>2</sub>, N<sub>2</sub>, CO, CO<sub>2</sub> and CH<sub>4</sub>. Calibration curves were determined separately by injecting  
50  
51 known quantities of pure gas. From product quantification TON and TOF were calculated using  
52  
53 eqs. 1 and 2 respectively.  
54  
55  
56  
57  
58  
59  
60

$$\text{TON} = \frac{n_{\text{product}}}{n_{\text{catalyst in the film}}} \quad (1)$$

$$\text{TOF} = \frac{\text{TON}}{t} \quad (2)$$

Since the electrolysis experiments shown are not conducted until total deactivation of the catalyst, the given TON value can only be regarded as a lower estimation of the actual value. The amount of electrochemically active molecular catalyst can be an order of magnitude smaller than the amount of catalyst present at the electrode. It may also lead to an underestimated value of the calculated TON.<sup>[63]</sup> Calculations of TON and TOF are made considering the total amount of molecular catalyst added into the catalyst material. Because the amount of active catalyst in the film is decaying over time, the TOF value is an apparent, averaged estimation.

**Material characterization.** Thin-film structural properties were determined by X-ray diffraction under grazing incidence (GIXRD) conditions for crystallinity determination and phase detection with a PANalytical Empyrean equipment using Cu-K $\alpha$  radiations. Thin-film morphologies were obtained using a Merlin VP Compact scanning electron microscope (SEM) provided by Zeiss, equipped with an energy dispersive X-Ray spectroscopy (EDS) detector from Bruker. Transmittance and Absorbance spectra were obtained using an Agilent Cary 5000 UV-Vis-NIR spectrophotometer equipped with an Agilent diffuse reflectance accessory. X-Ray Photoelectron Spectrometer analyses (XPS) were performed with a THERMO-VG ESCALAB 250 (RX source K Al (1486.6 eV)). Inductively coupled plasma (ICP) analyses were performed for the determination of the cobalt catalyst concentration into the films. The prepared thin layers were dissolved from the electrode using an acid solution 69% HNO<sub>3</sub>. The resulting solution was then diluted to 2% HNO<sub>3</sub> and injected into a ICAP 6300 Thermoelectron apparatus with detection of cobalt (238.8 nm).

**Chemical characterization.** NMR spectrum was recorded in DMSO-d<sub>6</sub> on a Varian 500 MHz spectrometer. Infrared spectra (FT-IR) were recorded on a Bio-Rad FTS 175C FTIR

1  
2  
3 spectrophotometer. UV-visible absorption spectra were obtained using a Shimadzu 2001 UV  
4 spectrophotometer. High resolution mass spectra were measured on an Agilent 6530 Accurate-  
5 Mass Q-TOF LC/MS spectrometer equipped with electrospray ionization (ESI) source.  
6  
7  
8  
9  
10

11 **Supporting Information.** Complementary characterization of ZnO layers (SEM, UV-Vis,  
12 EDX, XPS, AT-IR), Cyclic voltammetry and CPE experiments, Characterization of catalytic  
13 electrodes before and after electrolysis (Zn LMM Auger spectra, XRD), Catalyst synthesis  
14 characterizations (FT-IR, <sup>1</sup>H NMR, Uv-Vis).  
15  
16  
17  
18  
19  
20  
21  
22

### 23 **Author information**

#### 24 **Corresponding Authors**

25  
26  
27  
28 **Umit Isci** – Marmara University, Faculty of Technology, Department of Metallurgical &  
29 Materials Engineering, 34722 Istanbul, Türkiye; Email: [umit.isci@marmara.edu.tr](mailto:umit.isci@marmara.edu.tr)  
30  
31

32  
33  
34 **Negar Naghavi** – Institut Photovoltaïque d'Île-de-France (IPVF), CNRS, UMR 9006, 91120  
35 Palaiseau, France; Email: [negar.naghavi@chimieparistech.psl.eu](mailto:negar.naghavi@chimieparistech.psl.eu)  
36  
37

38  
39 **Marc Robert** – Université Paris Cité, Laboratoire d'Electrochimie Moléculaire, CNRS, F-  
40 75013 Paris, France; Institut Universitaire de France (IUF), F-75005 Paris, France. Email:  
41 [robert@u-paris.fr](mailto:robert@u-paris.fr)  
42  
43  
44

#### 45 **Authors**

46  
47  
48 **Julian Guerrero** – Université Paris Cité, Laboratoire d'Electrochimie Moléculaire, CNRS, F-  
49 75013 Paris, France; Institut Photovoltaïque d'Île-de-France (IPVF), CNRS, UMR 9006, 91120  
50 Palaiseau, France.  
51  
52  
53

54  
55 **Nathanaelle Schneider** – Institut Photovoltaïque d'Île-de-France (IPVF), CNRS, UMR 9006,  
56 91120 Palaiseau, France.  
57  
58  
59  
60

1  
2  
3 **Fabienne Dumoulin** – Acıbadem Mehmet Ali Aydınlar University, Faculty of Engineering and  
4  
5 Natural Sciences, Biomedical Engineering Department, 34752 Ataşehir, Istanbul, Türkiye  
6

7 **Daniel Lincot**– Institut Photovoltaïque d’Île-de-France (IPVF), CNRS, UMR 9006, 91120  
8  
9 Palaiseau, France.  
10  
11  
12

### 13 14 **Author Contributions**

15  
16 The manuscript was written through contributions of all authors. All authors have given  
17  
18 approval to the final version of the manuscript.  
19  
20  
21

### 22 23 **Notes**

24  
25 The authors declare no competing financial interest.  
26  
27  
28  
29

### 30 31 **Acknowledgements**

32  
33 The authors are very grateful for the financial support from the CNRS through the 80|Prime  
34  
35 program. M.R. acknowledges the Institut Universitaire de France (IUF) for partial financial  
36  
37 support.  
38  
39  
40

### 41 42 **References**

- 43  
44 (1) Kayan, A. Inorganic–Organic Hybrid Materials and Their Adsorbent Properties. *Adv*  
45  
46 *Compos Hybrid Mater* **2019**, 2 (1), 34–45. <https://doi.org/10.1007/s42114-018-0073-y>.  
47  
48 (2) Ananikov, V. P. Organic–Inorganic Hybrid Nanomaterials. *Nanomaterials* **2019**, 9 (9),  
49  
50 1197. <https://doi.org/10.3390/nano9091197>.  
51  
52 (3) Chongdar, S.; Bhattacharjee, S.; Bhanja, P.; Bhaumik, A. Porous Organic–Inorganic  
53  
54 Hybrid Materials for Catalysis, Energy and Environmental Applications. *Chem.*  
55  
56 *Commun.* **2022**, 58 (21), 3429–3460. <https://doi.org/10.1039/D1CC06340E>.  
57  
58  
59  
60

- 1  
2  
3 (4) Sun, Y.; Wang, F.; Fu, Y.; Chen, C.; Wang, X.; Xiao, Z.; Liu, Y.; Xu, J.; Li, B.; Wang,  
4 L. Two New Inorganic–Organic Hybrid Zinc Phosphites and Their Derived ZnO/ZnS  
5 Heterostructure for Efficient Photocatalytic Hydrogen Production. *RSC Adv.* **2020**, *10*  
6 (2), 812–817. <https://doi.org/10.1039/C9RA06919D>.  
7  
8  
9  
10  
11  
12 (5) Li, M.; Garg, S.; Chang, X.; Ge, L.; Li, L.; Konarova, M.; Rufford, T. E.; Rudolph, V.;  
13 Wang, G. Toward Excellence of Transition Metal-Based Catalysts for CO<sub>2</sub>  
14 Electrochemical Reduction: An Overview of Strategies and Rationales. *Small Methods*  
15 **2020**, *4* (7), 2000033. <https://doi.org/10.1002/smt.202000033>.  
16  
17  
18  
19  
20  
21 (6) Li, T.-T.; Mei, Y.; Li, H.; Qian, J.; Wu, M.; Zheng, Y.-Q. Highly Selective and Active  
22 Electrochemical Reduction of CO<sub>2</sub> to CO on a Polymeric Co(II)  
23 Phthalocyanine@Graphitic Carbon Nitride Nanosheet–Carbon Nanotube Composite.  
24 *Inorg. Chem.* **2020**, *59* (19), 14184–14192.  
25  
26  
27  
28  
29  
30  
31  
32  
33  
34 (7) Kinzel, N. W.; Werlé, C.; Leitner, W. Transition Metal Complexes as Catalysts for the  
35 Electroconversion of CO<sub>2</sub>: An Organometallic Perspective. *Angew. Chem. Int. Ed.* **2021**,  
36 anie.202006988. <https://doi.org/10.1002/anie.202006988>.  
37  
38  
39  
40 (8) Leung, C.-F.; Ho, P.-Y. Molecular Catalysis for Utilizing CO<sub>2</sub> in Fuel Electro-  
41 Generation and in Chemical Feedstock. *Catalysts* **2019**, *9* (9), 760.  
42  
43  
44  
45  
46  
47 (9) Dalle, K. E.; Warnan, J.; Leung, J. J.; Reuillard, B.; Karmel, I. S.; Reisner, E. Electro-  
48 and Solar-Driven Fuel Synthesis with First Row Transition Metal Complexes. *Chem.*  
49 *Rev.* **2019**, *119* (4), 2752–2875. <https://doi.org/10.1021/acs.chemrev.8b00392>.  
50  
51  
52  
53  
54 (10) Wang, M.; Torbensen, K.; Salvatore, D.; Ren, S.; Joulié, D.; Dumoulin, F.; Mendoza,  
55 D.; Lassalle-Kaiser, B.; Işci, U.; Berlinguette, C. P.; Robert, M. CO<sub>2</sub> Electrochemical  
56 Catalytic Reduction with a Highly Active Cobalt Phthalocyanine. *Nat Commun* **2019**, *10*  
57 (1), 3602. <https://doi.org/10.1038/s41467-019-11542-w>.  
58  
59  
60

- 1  
2  
3 (11) Ren, S.; Joulié, D.; Salvatore, D.; Torbensen, K.; Wang, M.; Robert, M.; Berlinguette, C.  
4  
5 P. Molecular Electrocatalysts Can Mediate Fast, Selective CO<sub>2</sub> Reduction in a Flow  
6  
7 Cell. **2019**, 4.  
8  
9  
10 (12) Cheng, D.; Zhao, Z.-J.; Zhang, G.; Yang, P.; Li, L.; Gao, H.; Liu, S.; Chang, X.; Chen,  
11  
12 S.; Wang, T.; Ozin, G. A.; Liu, Z.; Gong, J. The Nature of Active Sites for Carbon  
13  
14 Dioxide Electroreduction over Oxide-Derived Copper Catalysts. *Nat Commun* **2021**, 12  
15  
16 (1), 395. <https://doi.org/10.1038/s41467-020-20615-0>.  
17  
18  
19 (13) Pander, J. E.; Ren, D.; Huang, Y.; Loo, N. W. X.; Hong, S. H. L.; Yeo, B. S.  
20  
21 Understanding the Heterogeneous Electrocatalytic Reduction of Carbon Dioxide on  
22  
23 Oxide-Derived Catalysts. *ChemElectroChem* **2018**, 5 (2), 219–237.  
24  
25 <https://doi.org/10.1002/celec.201701100>.  
26  
27  
28 (14) Dattila, F.; García-Muelas, R.; López, N. Active and Selective Ensembles in Oxide-  
29  
30 Derived Copper Catalysts for CO<sub>2</sub> Reduction. *ACS Energy Lett.* **2020**, 5 (10), 3176–  
31  
32 3184. <https://doi.org/10.1021/acseenergylett.0c01777>.  
33  
34  
35 (15) Verdaguer-Casadevall, A.; Li, C. W.; Johansson, T. P.; Scott, S. B.; McKeown, J. T.;  
36  
37 Kumar, M.; Stephens, I. E. L.; Kanan, M. W.; Chorkendorff, I. Probing the Active  
38  
39 Surface Sites for CO Reduction on Oxide-Derived Copper Electrocatalysts. *J. Am.*  
40  
41 *Chem. Soc.* **2015**, 137 (31), 9808–9811. <https://doi.org/10.1021/jacs.5b06227>.  
42  
43  
44 (16) Kostecki, R.; Augustynski, J. Electrochemical Reduction of CO<sub>2</sub> at an Activated Silver  
45  
46 Electrode. *Berichte der Bunsengesellschaft für physikalische Chemie* **1994**, 98 (12),  
47  
48 1510–1515. <https://doi.org/10.1002/bbpc.19940981203>.  
49  
50  
51 (17) Ma, M.; Trzeźniewski, B. J.; Xie, J.; Smith, W. A. Selective and Efficient Reduction of  
52  
53 Carbon Dioxide to Carbon Monoxide on Oxide-Derived Nanostructured Silver  
54  
55 Electrocatalysts. *Angew. Chem. Int. Ed.* **2016**, 55 (33), 9748–9752.  
56  
57 <https://doi.org/10.1002/anie.201604654>.  
58  
59  
60

- 1  
2  
3 (18) Bi, Q.; Huang, X.; Yin, G.; Chen, T.; Du, X.; Cai, J.; Xu, J.; Liu, Z.; Han, Y.; Huang, F.  
4  
5 Cooperative Catalysis of Nickel and Nickel Oxide for Efficient Reduction of CO<sub>2</sub> to  
6  
7 CH<sub>4</sub>. *ChemCatChem* **2019**, *11* (4), 1295–1302. <https://doi.org/10.1002/cctc.201801896>.  
8  
9
- 10 (19) Wang, Z.; Fan, Jiajie; Cheng, Bei; Yu, Jiaguo; Xu, Jingsan. Nickel-Based Cocatalysts  
11  
12 for Photocatalysis: Hydrogen Evolution, Overall Water Splitting and CO<sub>2</sub> Reduction.  
13  
14 *Materials Today Physics* **2020**, *15*, 27. <https://doi.org/10.1016/j.mtphys.2020.100279>.  
15  
16
- 17 (20) Dey, G. R.; Belapurkar, A. D.; Kishore, K. Photo-Catalytic Reduction of Carbon  
18  
19 Dioxide to Methane Using TiO<sub>2</sub> as Suspension in Water. *Journal of Photochemistry and*  
20  
21 *Photobiology A: Chemistry* **2004**, *163* (3), 503–508.  
22  
23 <https://doi.org/10.1016/j.jphotochem.2004.01.022>.  
24  
25
- 26 (21) Shehzad, N.; Tahir, M.; Johari, K.; Murugesan, T.; Hussain, M. A Critical Review on  
27  
28 TiO<sub>2</sub> Based Photocatalytic CO<sub>2</sub> Reduction System: Strategies to Improve Efficiency.  
29  
30 *Journal of CO<sub>2</sub> Utilization* **2018**, *26*, 98–122. <https://doi.org/10.1016/j.jcou.2018.04.026>.  
31  
32
- 33 (22) Jin, L.; Shaaban, E.; Bamonte, S.; Cintron, D.; Shuster, S.; Zhang, L.; Li, G.; He, J.  
34  
35 Surface Basicity of Metal@TiO<sub>2</sub> to Enhance Photocatalytic Efficiency for CO<sub>2</sub>  
36  
37 Reduction. *ACS Appl. Mater. Interfaces* **2021**, *13* (32), 38595–38603.  
38  
39 <https://doi.org/10.1021/acsami.1c09119>.  
40  
41
- 42 (23) Djurišić, A. B.; Leung, Y. H. Optical Properties of ZnO Nanostructures. *Small* **2006**, *2*  
43  
44 (8–9), 944–961. <https://doi.org/10.1002/sml.200600134>.  
45  
46
- 47 (24) Rezaie, M. N.; Mohammadnejad, S.; Ahadzadeh, S. Hybrid Inorganic-Organic Light-  
48  
49 Emitting Heterostructure Devices Based on ZnO. *Optics & Laser Technology* **2021**, *138*,  
50  
51 106896. <https://doi.org/10.1016/j.optlastec.2020.106896>.  
52  
53
- 54 (25) Kao, M.-C.; Chen, H.-Z.; Young, S.-L.; Lin, C.-C.; Kung, C.-Y. Structure and  
55  
56 Photovoltaic Properties of ZnO Nanowire for Dye-Sensitized Solar Cells. *Nanoscale Res*  
57  
58 *Lett* **2012**, *7* (1), 260. <https://doi.org/10.1186/1556-276X-7-260>.  
59  
60

- 1  
2  
3 (26) Manor, A.; Katz, E. A.; Tromholt, T.; Krebs, F. C. Enhancing Functionality of ZnO Hole  
4  
5 Blocking Layer in Organic Photovoltaics. *Solar Energy Materials and Solar Cells* **2012**,  
6  
7 98, 491–493. <https://doi.org/10.1016/j.solmat.2011.11.026>.  
8  
9  
10 (27) Sharma, A.; Franklin, J. B.; Singh, B.; Andersson, G. G.; Lewis, D. A. Electronic and  
11  
12 Chemical Properties of ZnO in Inverted Organic Photovoltaic Devices. *Organic*  
13  
14 *Electronics* **2015**, 24, 131–136. <https://doi.org/10.1016/j.orgel.2015.05.032>.  
15  
16  
17 (28) Luo, W.; Zhang, Q.; Zhang, J.; Moiola, E.; Zhao, K.; Züttel, A. Electrochemical  
18  
19 Reconstruction of ZnO for Selective Reduction of CO<sub>2</sub> to CO. *Applied Catalysis B:*  
20  
21 *Environmental* **2020**, 273, 119060. <https://doi.org/10.1016/j.apcatb.2020.119060>.  
22  
23  
24 (29) Han, K.; Ngene, P.; Jongh, P. Structure Dependent Product Selectivity for CO<sub>2</sub>  
25  
26 Electroreduction on ZnO Derived Catalysts. *ChemCatChem* **2021**, 13 (8), 1998–2004.  
27  
28 <https://doi.org/10.1002/cctc.202001710>.  
29  
30  
31 (30) Raula, M.; Rashid, Md. H.; Paira, T. K.; Dinda, E.; Mandal, T. K. Ascorbate-Assisted  
32  
33 Growth of Hierarchical ZnO Nanostructures: Sphere, Spindle, and Flower and Their  
34  
35 Catalytic Properties. *Langmuir* **2010**, 26 (11), 8769–8782.  
36  
37 <https://doi.org/10.1021/la904507q>.  
38  
39  
40 (31) Kumar, S.; Kumar, A.; Kumar, A.; Krishnan, V. Nanoscale Zinc Oxide Based  
41  
42 Heterojunctions as Visible Light Active Photocatalysts for Hydrogen Energy and  
43  
44 Environmental Remediation. *Catalysis Reviews* **2020**, 62 (3), 346–405.  
45  
46 <https://doi.org/10.1080/01614940.2019.1684649>.  
47  
48  
49 (32) Jiang, X.; Cai, F.; Gao, D.; Dong, J.; Miao, S.; Wang, G.; Bao, X. Electrocatalytic  
50  
51 Reduction of Carbon Dioxide over Reduced Nanoporous Zinc Oxide. *Electrochemistry*  
52  
53 *Communications* **2016**, 68, 67–70. <https://doi.org/10.1016/j.elecom.2016.05.003>.  
54  
55  
56 (33) Jehl, Z.; Rousset, J.; Donsanti, F.; Renou, G.; Naghavi, N.; Lincot, D. Electrodeposition  
57  
58 of ZnO Nanorod Arrays on ZnO Substrate with Tunable Orientation and Optical  
59  
60

- 1  
2  
3 Properties. *Nanotechnology* **2010**, *21* (39), 395603. [https://doi.org/10.1088/0957-](https://doi.org/10.1088/0957-4484/21/39/395603)  
4  
5 4484/21/39/395603.  
6  
7  
8 (34) Pauporté, Th.; Bataille, G.; Joulaud, L.; Vermersch, F. J. Well-Aligned ZnO Nanowire  
9  
10 Arrays Prepared by Seed-Layer-Free Electrodeposition and Their Cassie–Wenzel  
11  
12 Transition after Hydrophobization. *J. Phys. Chem. C* **2010**, *114* (1), 194–202.  
13  
14 <https://doi.org/10.1021/jp9087145>.  
15  
16  
17 (35) Choi, K.-S.; Chang, S.-P. Effect of Structure Morphologies on Hydrogen Gas Sensing by  
18  
19 ZnO Nanotubes. *Materials Letters* **2018**, *230*, 48–52.  
20  
21 <https://doi.org/10.1016/j.matlet.2018.07.031>.  
22  
23  
24 (36) Pelicano, C. M.; Yanagi, H. Enhanced Charge Transport in Al-Doped ZnO Nanotubes  
25  
26 Designed *via* Simultaneous Etching and Al Doping of H<sub>2</sub>O-Oxidized ZnO Nanorods for  
27  
28 Solar Cell Applications. *J. Mater. Chem. C* **2019**, *7* (16), 4653–4661.  
29  
30 <https://doi.org/10.1039/C9TC00401G>.  
31  
32  
33 (37) Kim, K.; Choi, P. gyu; Itoh, T.; Masuda, Y. Atomic Step Formation on Porous ZnO  
34  
35 Nanobelts: Remarkable Promotion of Acetone Gas Detection up to the Parts per Trillion  
36  
37 Level. *J. Mater. Chem. A* **2022**, *10* (26), 13839–13847.  
38  
39 <https://doi.org/10.1039/D2TA02789E>.  
40  
41  
42 (38) Hong, M.; Meng, J.; Yu, H.; Du, J.; Ou, Y.; Liao, Q.; Kang, Z.; Zhang, Z.; Zhang, Y.  
43  
44 Ultra-Stable ZnO Nanobelts in Electrochemical Environments. *Mater. Chem. Front.*  
45  
46 **2021**, *5* (1), 430–437. <https://doi.org/10.1039/D0QM00709A>.  
47  
48  
49 (39) Taunk, P. B.; Das, R.; Bisen, D. P.; Tamrakar, R. K.; Rathor, N. Synthesis and Optical  
50  
51 Properties of Chemical Bath Deposited ZnO Thin Film. *Karbala International Journal*  
52  
53 *of Modern Science* **2015**, *1* (3), 159–165. <https://doi.org/10.1016/j.kijoms.2015.11.002>.  
54  
55  
56 (40) Sánchez-Martín, S.; Olaizola, S. M.; Castaño, E.; Urionabarrenetxea, E.; Mandayo, G.  
57  
58 G.; Ayerdi, I. Study of Deposition Parameters and Growth Kinetics of ZnO Deposited by  
59  
60

- 1  
2  
3 Aerosol Assisted Chemical Vapor Deposition. *RSC Adv.* **2021**, *11* (30), 18493–18499.  
4  
5 <https://doi.org/10.1039/D1RA03251H>.  
6  
7  
8 (41) Nozik, A.J. Photoelectrochemical cells. *Phil. Trans. R. Soc. Lond. A.* **1980**, *295*, 453–470.  
9  
10 <http://doi.org/10.1098/rsta.1980.0141>  
11  
12 (42) Peulon, S.; Lincot, D. Cathodic Electrodeposition from Aqueous Solution of Dense or  
13  
14 Open-Structured Zinc Oxide Films. *Adv. Mater.* **1996**, *8* (2), 166–170.  
15  
16 <https://doi.org/10.1002/adma.19960080216>.  
17  
18  
19 (43) Izaki, M.; Omi, T. Transparent Zinc Oxide Films Prepared by Electrochemical Reaction.  
20  
21 *Appl. Phys. Lett.* **1996**, *68* (17), 2439–2440. <https://doi.org/10.1063/1.116160>.  
22  
23  
24 (44) Yoshida, T.; Minoura, H. Electrochemical Self-Assembly of Dye-Modified Zinc Oxide  
25  
26 Thin Films. *Adv. Mater.* **2000**, No. 16, 4. [https://doi.org/10.1002/1521-](https://doi.org/10.1002/1521-4095(200008)12:16<1219::AID-ADMA1219>3.0.CO;2-5)  
27  
28 [4095\(200008\)12:16<1219::AID-ADMA1219>3.0.CO;2-5](https://doi.org/10.1002/1521-4095(200008)12:16<1219::AID-ADMA1219>3.0.CO;2-5)  
29  
30  
31 (45) Haller, S.; Suguira, T.; Lincot, D.; Yoshida, T. Design of a Hierarchical Structure of  
32  
33 ZnO by Electrochemistry for ZnO-Based Dye-Sensitized Solar Cells: Design of a  
34  
35 Hierarchical Structure of ZnO by Electrochemistry. *phys. stat. sol. (a)* **2010**, *207* (10),  
36  
37 2252–2257. <https://doi.org/10.1002/pssa.201026140>.  
38  
39  
40 (46) Yoshida, T.; Tochimoto, M.; Schlettwein, D.; Wöhrle, D.; Sugiura, T.; Minoura, H. Self-  
41  
42 Assembly of Zinc Oxide Thin Films Modified with Tetrasulfonated  
43  
44 Metallophthalocyanines by One-Step Electrodeposition. *Chem. Mater.* **1999**, *11* (10),  
45  
46 2657–2667. <https://doi.org/10.1021/cm980619o>.  
47  
48  
49 (47) Pauporté, T.; Yoshida, T.; Cortès, R.; Froment, M.; Lincot, D. Electrochemical Growth  
50  
51 of Epitaxial Eosin/ZnO Hybrid Films. *J. Phys. Chem. B* **2003**, *107* (37), 10077–10082.  
52  
53 <https://doi.org/10.1021/jp034079g>.  
54  
55  
56 (48) Pauporté, T.; Bedioui, F.; Lincot, D. Nanostructured Zinc Oxide–Chromophore Hybrid  
57  
58 Films with Multicolored Electrochromic Properties. *J. Mater. Chem.* **2005**, *15* (15),  
59  
60 1552–1559. <https://doi.org/10.1039/B416419A>.

- 1  
2  
3 (49) Yang, H.; Wang, X.; Hu, Q.; Chai, X.; Ren, X.; Zhang, Q.; Liu, J.; He, C. Recent  
4  
5 Progress in Self-Supported Catalysts for CO<sub>2</sub> Electrochemical Reduction. *Small*  
6  
7 *Methods* **2020**, *4* (6), 1900826. <https://doi.org/10.1002/smt.201900826>.  
8  
9
- 10 (50) Basnet, P.; Samanta, D.; Inakhunbi Chanu, T.; Mukherjee, J.; Chatterjee, S. Assessment  
11  
12 of Synthesis Approaches for Tuning the Photocatalytic Property of ZnO Nanoparticles.  
13  
14 *SN Appl. Sci.* **2019**, *1* (6), 633. <https://doi.org/10.1007/s42452-019-0642-x>.  
15  
16
- 17 (51) Höchst, H.; Goldmann, A.; Hüfner, S.; Malter, H. X-Ray Photoelectron Valence Band  
18  
19 Studies on Phthalocyanine Compounds. *Physica Status Solidi b*, **1976**, *76*, 559-  
20  
21 586. <https://doi.org/10.1002/pssb.2220760215>  
22  
23
- 24 (52) Hellgren, N.; Guo, J.; Luo, Y.; Sâthe, C.; Agui, A.; Kashtanov, S.; Nordgren, J.; Ågren,  
25  
26 H.; Sundgren, J.-E. Electronic Structure of Carbon Nitride Thin Films Studied by X-Ray  
27  
28 Spectroscopy Techniques. *Thin Solid Films* **2005**, *471* (1–2), 19–34.  
29  
30 <https://doi.org/10.1016/j.tsf.2004.03.027>.  
31  
32
- 33 (53) Neelgund, G. M.; Oki, A. Cobalt Phthalocyanine-Sensitized Graphene–ZnO Composite:  
34  
35 An Efficient Near-Infrared-Active Photothermal Agent. *ACS Omega* **2019**, *4* (3), 5696–  
36  
37 5704. <https://doi.org/10.1021/acsomega.8b03222>.  
38  
39
- 40 (54) Luo, W.; Zhang, Q.; Zhang, J.; Moioli, E.; Zhao, K.; Züttel, A. Electrochemical  
41  
42 Reconstruction of ZnO for Selective Reduction of CO<sub>2</sub> to CO. *Applied Catalysis B:*  
43  
44 *Environmental* **2020**, *273*, 119060. <https://doi.org/10.1016/j.apcatb.2020.119060>.  
45  
46
- 47 (55) Geng, Z.; Kong, X.; Chen, W.; Su, H.; Liu, Y.; Cai, F.; Wang, G.; Zeng, J. Oxygen  
48  
49 Vacancies in ZnO Nanosheets Enhance CO<sub>2</sub> Electrochemical Reduction to CO. *Angew.*  
50  
51 *Chem.* **2018**, *130* (21), 6162–6167. <https://doi.org/10.1002/ange.201711255>.  
52  
53
- 54 (56) Xiang, Q.; Li, F.; Wang, J.; Chen, W.; Miao, Q.; Zhang, Q.; Tao, P.; Song, C.; Shang,  
55  
56 W.; Zhu, H.; Deng, T.; Wu, J. Heterostructure of ZnO Nanosheets/Zn with a Highly  
57  
58 Enhanced Edge Surface for Efficient CO<sub>2</sub> Electrochemical Reduction to CO. *ACS Appl.*  
59  
60 *Mater. Interfaces* **2021**, *13* (9), 10837–10844. <https://doi.org/10.1021/acsaami.0c20302>.

- 1  
2  
3 (57) Liu, K.; Wang, J.; Shi, M.; Yan, J.; Jiang, Q. Simultaneous Achieving of High Faradaic  
4 Efficiency and CO Partial Current Density for CO<sub>2</sub> Reduction via Robust,  
5 Noble-Metal-Free Zn Nanosheets with Favorable Adsorption Energy. *Adv. Energy*  
6 *Mater.* **2019**, *9* (21), 1900276. <https://doi.org/10.1002/aenm.201900276>.  
7  
8  
9  
10  
11  
12 (58) Zong, X.; Jin, Y.; Li, Y.; Zhang, X.; Zhang, S.; Xie, H.; Zhang, J.; Xiong, Y.  
13 Morphology-Controllable ZnO Catalysts Enriched with Oxygen-Vacancies for Boosting  
14 CO<sub>2</sub> Electroreduction to CO. *Journal of CO<sub>2</sub> Utilization* **2022**, *61*, 102051.  
15  
16  
17  
18  
19  
20  
21  
22 (59) Zhang, X.; Wu, Z.; Zhang, X.; Li, L.; Li, Y.; Xu, H.; Li, X.; Yu, X.; Zhang, Z.; Liang,  
23 Y.; Wang, H. Highly Selective and Active CO<sub>2</sub> Reduction Electrocatalysts Based on  
24 Cobalt Phthalocyanine/Carbon Nanotube Hybrid Structures. *Nat Commun* **2017**, *8* (1),  
25  
26  
27  
28  
29  
30  
31 (60) Mai, N. T.; Thuy, T. T.; Mott, D. M.; Maenosono, S. Chemical Synthesis of Blue-  
32 Emitting Metallic Zinc Nano-Hexagons. *CrystEngComm* **2013**, *15* (33), 6606.  
33  
34  
35  
36  
37  
38 (61) Le Tulzo, H.; Schneider, N.; Lincot, D.; Patriarche, G.; Donsanti, F. Impact of the  
39 Sequence of Precursor Introduction on the Growth and Properties of Atomic Layer  
40 Deposited Al-Doped ZnO Films. *Journal of Vacuum Science & Technology A* **2018**, *36*  
41  
42  
43  
44  
45  
46 (62) König, M.; Vaes, J.; Klemm, E.; Pant, D. Solvents and Supporting Electrolytes in the  
47 Electrochemical Reduction of CO<sub>2</sub>. *iScience* **2019**, *19*, 135–160.  
48  
49  
50  
51  
52  
53  
54 (63) Pati, P. B.; Wang, R.; Boutin, E.; Diring, S.; Jobic, S.; Barreau, N.; Odobel, F.; Robert,  
55 M. Photocathode Functionalized with a Molecular Cobalt Catalyst for Selective Carbon  
56 Dioxide Reduction in Water. *Nat Commun* **2020**, *11* (1), 3499.  
57  
58  
59  
60  
<https://doi.org/10.1038/s41467-020-17125-4>.

1  
2  
3  
4  
5  
6  
7  
8  
9  
10  
11  
12  
13  
14  
15  
16  
17  
18  
19  
20  
21  
22  
23  
24  
25  
26  
27  
28  
29  
30  
31  
32  
33  
34  
35  
36  
37  
38  
39  
40  
41  
42  
43  
44  
45  
46  
47  
48  
49  
50  
51  
52  
53  
54  
55  
56  
57  
58  
59  
60